AIP | The Journal of Chemical Physics

Pure bending dynamics in the acetylene 1Σg+ state up to 15000 cm−1 of internal energy

Matthew P. Jacobson, Jonathan P. O'Brien, Robert J. Silbey, and Robert W. Field

Citation: J. Chem. Phys. 109, 121 (1998); doi: 10.1063/1.476529
View online: http://dx.doi.org/10.1063/1.476529
View Table of Contents: http://jcp.aip.org/resource/1/JCPSA6/v109/i1
Published by the American Institute of Physics.

JOURNAL OF CHEMICAL PHYSICS VOLUME 109, NUMBER 1 1 JULY 1998

Pure bending dynamics in the acetylene $\tilde{X}\ ^1\Sigma_g^+$ state up to 15 000 cm^{-1} of internal energy

Matthew P. Jacobson, Jonathan P. O'Brien, Robert J. Silbey,
and Robert W. Field
Department of Chemistry and George R. Harrison Spectroscopy Laboratory,
Massachusetts Institute of Technology, Cambridge, Massachusetts 02139

(Received 3 February 1998; accepted 25 March 1998)

We investigate the large-amplitude bending dynamics of acetylene, in its ground electronic state, using an effective Hamiltonian model that reproduces all relevant experimental data, up to 15 000 cm^{-1} in internal energy, with 1.4 cm^{-1} accuracy (1σ). The experimental data which make this analysis possible are derived from the dispersed fluorescence (DF) data set that we recently reported [J. P. O'Brien *et al.*, J. Chem. Phys. **108**, 7100 (1998)] for the acetylene $\tilde{A}\ ^1A_u \rightarrow \tilde{X}\ ^1\Sigma_g^+$ system, which includes DF spectra recorded from five different vibrational levels of the $\tilde{A}\ ^1A_u$ state. A numerical pattern recognition technique has permitted the assignment of polyad quantum numbers to observed transitions in these spectra, with up to 15 000 cm^{-1} in internal energy. Here we analyze a special subset of the identified polyads, those which involve excitation exclusively in the *trans* and *cis* bending modes: the pure bending polyads. The bending dynamics that is encoded in these polyads is analyzed using both frequency and time-domain formalisms. Among the conclusions of this analysis is that, in many ways, the observed bending dynamics is somewhat simpler at 15 000 than it is at 10 000 cm^{-1}; this rather surprising result is explained in terms of qualitative changes in the structures of the pure bending polyads as a function of increasing internal energy. *© 1998 American Institute of Physics.* [S0021-9606(98)01425-1]

I. INTRODUCTION

This paper is intended as a contribution to the understanding of intramolecular vibrational energy exchange, when it is poorly described by either purely statistical models [i.e., Rice-Ramsperger-Kassel-Marcus (RRKM)] or purely separable models (i.e., harmonic oscillator/normal mode descriptions). The system described here is the bending dynamics of acetylene in its electronic ground state. Specifically, we present and analyze a model for the pure bending dynamics of acetylene that reproduces all available and relevant experimental data up to 15 000 cm^{-1} in internal energy (22 quanta of bending excitation). We hope that this system will be of general interest to experimentalists and theoreticians interested in unimolecular dynamics, both because acetylene is an important organic prototype molecule, and because very large amplitude motions of the molecule, at chemically significant internal energy, are accurately represented by the model we present.

The experimental data on which our model of acetylene bending dynamics is based consist primarily of the dispersed fluorescence (DF) spectra that have recently been recorded by our group.[1,2] Absorption spectroscopy has characterized many of the low-lying fundamental, overtone, and combination bands of the *trans* and *cis* modes of acetylene (i.e., below 3000 cm^{-1}),[3] but DF and SEP (stimulated emission pumping) spectroscopy have largely been responsible for characterizing the highly excited bending vibrational levels. These latter double resonance schemes utilize as intermediate states rovibrational levels of the $\tilde{A}\ ^1A_u$ state, which has a *trans*-bent equilibrium geometry, with a nominal CC double bond. The large change in geometry between the $\tilde{A}\ ^1A_u$ and $\tilde{X}\ ^1\Sigma_g^+$ electronic states results in a broad Franck-Condon profile in emission from the $\tilde{A}\ ^1A_u$ state, extending from ~3000 to >20 000 cm^{-1} of internal energy.

Our approach to extracting the bending dynamics of acetylene from these spectra consists of two steps: assignment of the spectra, followed by a fit of the assigned transitions to an effective Hamiltonian model. The assignments made in the first step of this process are not normal mode quantum numbers, which extensive intramolecular vibrational redistribution (IVR) renders meaningless for most vibrational energy levels at high internal energy, but rather *polyad* quantum numbers,[4–7] which represent approximately conserved vibrational quantities. The assignment of these quantum numbers to spectral features in the congested DF spectra has been made possible by two recent advances in our group, both of which have been reported previously. The first advance is the recording of an improved DF data set for acetylene $\tilde{A}\ ^1A_u \rightarrow \tilde{X}\ ^1\Sigma_g^+$ emission.[1,2] This data set consists of DF spectra recorded *via* the $^rQ_0(1)$, $J'_{K_a,K_c} = 1'_{1,0}$ excitation lines of the $V_0^0K_0^1$ (origin band), $V_0^1K_0^1$, $2_0^1V_0^1K_0^1$, $V_0^2K_0^1$, and $2_0^1V_0^2K_0^1$ vibrational bands (V represents the *trans* bending mode, v'_3 in the $\tilde{A}$ state and v''_4 in the $\tilde{X}$ state; ''2'' represents the CC stretch; and K has its conventional meaning as the unsigned body-fixed projection of the total angular momentum). The emission from each of these $\tilde{A}\ ^1A_u$ state intermediates was recorded at two different resolutions, ~7 cm^{-1} (recorded in second order of the grating) and 18 cm^{-1}

(recorded in first order), and thus the data set consists of ten different DF spectra. These spectra were subjected to rigorous frequency and intensity calibrations, such that each resolution element in the data set is calibrated to within ~ 3 cm^{-1} (2σ).

The second advance is a new approach to analyzing these DF spectra, which is based on a numerical pattern recognition technique that we have developed entitled eXtended Cross-Correlation (XCC).[2,8,9] Briefly, the approach is made possible by the existence of polyad quantum numbers in the acetylene $\tilde{X}\ ^1\Sigma_g^+$ state, which implies that the acetylene H^{eff} is, to a good approximation, block diagonal. Further, in the acetylene $\tilde{A}\ ^1A_u \rightarrow \tilde{X}\ ^1\Sigma_g^+$ system, the Franck-Condon active modes are, to a good approximation, CC-stretch and *trans* bend, and it can be demonstrated that in every polyad (block of the H^{eff}), there is at most one bright state of the form $(0,v_2,0,v_4,0)$. This fact leads to a powerful method for analyzing the IVR in the acetylene $\tilde{X}\ ^1\Sigma_g^+$ state. Namely, the existence of only one bright state per polyad implies that there are no interference effects between the bright states, and each bright state displays the same fractionation pattern within the corresponding polyad in each of the DF spectra. That is, as long as the polyad structure remains intact, each fractionated bright state can be considered to be a pattern that is repeated in multiple DF spectra, and the XCC-based approach permits the disentanglement of these fractionated bright state patterns from the spectra.

By utilizing this approach, the fractionation patterns of 38 bright states have been disentangled from the DF data set at E_{vib} up to 15 000 cm^{-1}. One subset of these bright states, those *without* excitation in the CC stretch, $(0,0,0,v_4,0)$, will be analyzed in detail in this paper. Together, the fractionation patterns of these bright states encode the short-time $(\sim 1$ ps) pure bending dynamics of acetylene with up to 22 quanta of bending excitation, and in this paper we report the development of an effective Hamiltonian which reproduces all of these pure bending fractionation patterns, in addition to all pure bending vibrational energy levels that were observed at lower internal energy by absorption spectroscopy. This H^{eff} is similar in structure to previously reported effective Hamiltonians,[3,10] but matches the available data to substantially higher internal energy $(\leqslant 15\,000\ \mathrm{cm}^{-1})$. Challenges which are inherent to fitting experimental data at such high internal energy necessitated new methodologies for performing the fit, which are described in Sec. III. The remainder of the paper is devoted to analyzing the pure bending dynamics of acetylene, as represented by the H^{eff}, from multiple perspectives. Time-dependent viewpoints on the dynamics are examined first, in Sec. IV, followed in Sec. V by a discussion of dilution factors, which are frequently used to quantify the extent of IVR. A framework for understanding the unexpectedly complicated and counterintuitive trends that are outlined in these two sections is presented in Sec. VI, which analyzes the structures of the pure bending polyads.

II. RESULTS

Figure 1 depicts a subset of the bright state fractionation patterns that were extracted, using numerical pattern recognition (XCC), from the DF data set reported in Ref. 2. The subset of fractionated bright states depicted here are progressions in the *trans* bend mode, $(0,0,0,v_4,0)$, with zero quanta of excitation in all other modes. These bright states are not eigenstates of the molecular Hamiltonian (although at very low internal energy they approximate eigenstates), and the fractionation patterns in Fig. 1 represent the distribution of bright state character among the eigenstates. As explained in the Introduction, the existence of polyads, which is requisite for the success of the pattern recognition approach, implies that the character of any single bright state can only be distributed among the eigenstates that belong to a single polyad.

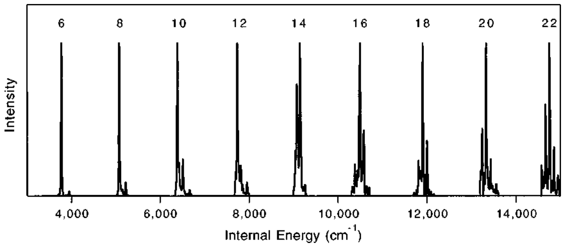

FIG. 1. Fractionated pure bending bright state patterns, $(0,0,0,v_4{}^{0/2},0^0)$, labeled according to v_4, that have been extracted from the dispersed fluorescence data set using numerical pattern recognition (XCC) (see Refs. 2, 8, and 9).

The polyad quantum numbers for the acetylene $\tilde{X}\ ^1\Sigma_g^+$ state are,

$$N_{\mathrm{res}} = 5v_1 + 3v_2 + 5v_3 + v_4 + v_5,$$

$$N_s = v_1 + v_2 + v_3,$$

$$l = l_4 + l_5.$$

The physical meanings of the N_s and l quantum numbers are simple; they represent the total number of quanta of stretching excitation and the total vibrational angular momentum, respectively. The N_{res} quantum number has a slightly more subtle meaning; it reflects the approximate ratios among the normal mode frequencies, and thus represents a restriction under which only states with approximately the same zero-order energy may interact.

Since the bright states that are depicted in Fig. 1 have zero quanta of excitation in all of the stretching modes, they all belong to polyads with $N_s = 0$, which we refer to as pure bending polyads. For this set of polyads, the N_{res} quantum number simplifies to

$$N_{\mathrm{res}} = v_4 + v_5 = N_b,$$

in which we have introduced N_b, the number of quanta of bending excitation, as a shorthand notation for the N_{res} and N_s polyad numbers for the pure bending polyads. It should also be noted that g/u symmetry with respect to the center of inversion is conserved by the known anharmonic resonances, and thus can also be used to label eigenstates, as well as the rigorously conserved total angular momentum quantum number, J, and parity, which can be labeled using either the $+/-$ or e/f conventions. Thus, to identify a pure bending polyad uniquely, a total of five labels need to be specified: N_b, l, J, g/u, and parity.

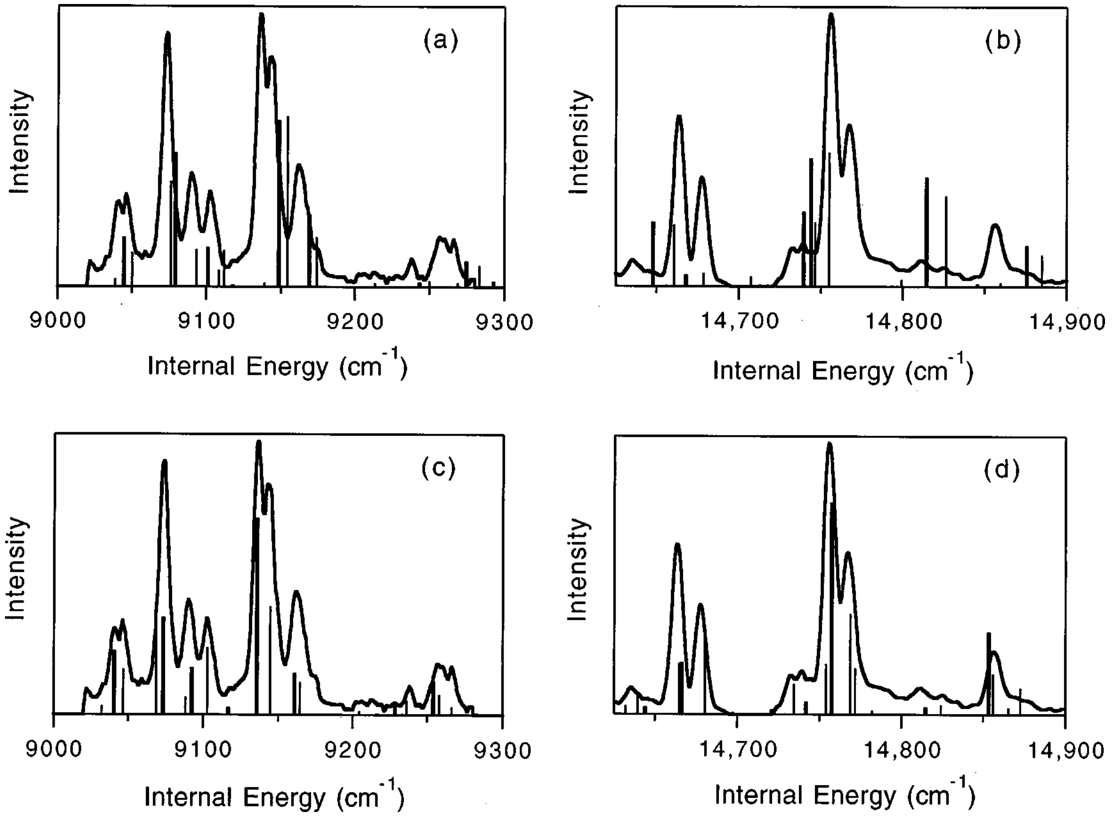

FIG. 2. Comparison of predictions of the H^{eff} (vertical lines) with the experimentally observed fractionated bright states (solid line). The thick vertical lines correspond to ($J=1$, $l=0$, e parity); the thin vertical lines represent ($J=2$, $l=2$, f parity). Panels (a) and (b) depict the predictions of the THSOF H^{eff} model, while panels (c) and (d) depict the predictions of the refined H^{eff} reported here.

Selection rules for electronic transitions specify that all polyads observed in the DF data set possess g symmetry with respect to the center of inversion. The values of the angular momentum quantum numbers, J and l, are determined by selection rules. The DF spectra, from which the fractionated bright states in Fig. 1 were extracted, were all recorded using excitation of $Q(1)$ rotational transitions (in ''cold'' absorption bands), and thus the intermediate rotational state selected has ($J'=1$, $K'=1$, f parity). The emission from the selected $\tilde{A}\ {}^1A_u$ state rovibrational levels thus consists of two rotational components, ($J=1$, $l=0$, e parity), and ($J=2$, $l=2$, f parity), meaning that for every value of N_b, a pair of polyads, $l=0,2$, are observed experimentally. The relative intensities of the fractionated bright state patterns for these two sets of polyads can be determined using direction cosine matrix elements, and because this ratio is invariant among the DF spectra, the numerical pattern recognition algorithms (XCC) extract the $l=0,2$ *pair* of fractionated bright states (for the same value of N_b) as a *single pattern*. Note, however, that this property of the pattern recognition analysis does not imply any constructive/destructive interference between the $l=0$ and 2 bright states, and it will be seen below that an effective Hamiltonian can be used to apportion individual lines within the extracted pattern between the $l=0$ and $l=2$ polyads.

III. REFINEMENT OF THE PURE BENDING H^{eff}

One of the earliest effective Hamiltonians for the pure bending levels of acetylene was defined by Josef Plíva.[3] This H^{eff} included 40 molecular constants that were fit to ~1200 rovibrational levels of the $\tilde{X}\ {}^1\Sigma_g^+$ state that had been observed by infrared absorption spectroscopy, with a standard deviation of 0.006 cm^{-1}. All of the rovibrational levels included in Plíva's fit lay below 3000 cm^{-1} of internal energy, and thus the parameters from that work cannot be expected to represent accurately the highly excited bending levels that are the subject of the present study.

More recently, an effective Hamiltonian has been reported by Abbouti Temsamani, Herman, Solina, O'Brien, and Field[10] (hereafter referred to as THSOF) which reproduces the energies of 41 bending vibrational levels of acetylene (up to 8000 cm^{-1}) to ± 0.35 cm^{-1} (1σ) accuracy. The THSOF H^{eff} resulted from minor modifications of an H^{eff} previously described by Abbouti Temsamani and Herman,[11] which was fit to 122 vibrational levels with $E_{vib} < 12\,000$ cm^{-1}, primarily with $N_s \neq 0$. It is also worth noting that the terms included in the THSOF bending H^{eff} are nearly identical to those included by Plíva.

The THSOF H^{eff} has been demonstrated to have substantial predictive power at energies higher than the levels included in the fit. Specifically, as can be seen in Fig. 2(a), the THSOF H^{eff} reproduces the key qualitative features of the $(0,0,0,14^{0/2},0^0)$ fractionated bright state. There is a one-to-one correspondence between the intense transitions predicted by the H^{eff} (sticks) and the observed transitions (solid line). The predicted and observed eigenenergies differ by up to 15 cm^{-1}, but the pattern of relative intensities predicted by the H^{eff} bears a strong qualitative resemblance to the DF data.

It should be noted that a discrepancy between the THSOF H^{eff} model and the experimental data for this polyad, which was discussed in Ref. 10, has now been resolved. The peak at 8945 cm^{-1} in Fig. 2 of Ref. 10, which deviated substantially from the predictions of the H^{eff} was, in fact, misassigned previously. Recent experimental work,[2] which is the basis for the results presented in this paper, proved that this peak is not assignable to *any* of the expected polyads at this internal energy, and thus this peak has been classified as an ''extra pattern,'' the origin of which is still under investigation (although it is believed that the extra features do not arise from acetylene $\tilde{A}\rightarrow\tilde{X}$ emission).[12]

Above 10 000 cm^{-1}, the agreement between the THSOF H^{eff} and the experimental data degrades substantially. Figure 2(b) depicts the agreement for the $(0,0,0,22^{0/2},0^0)$ fractionated bright state. The THSOF H^{eff} predicts a pattern of eight intense peaks, whereas only five intense peaks are observed experimentally. Of course, it is not reasonable to expect an H^{eff} which has been fit to data only up to 8000 cm^{-1} to have substantial predictive power at 15 000 cm^{-1}. For this reason, we have performed a refinement of the THSOF H^{eff}, which utilizes all of the experimental data that were previously included in the THSOF fit, plus 42 new pure bending vibrational levels, with up to 15 000 cm^{-1} of internal energy, which were identified in our DF data set as described in the preceding section. Thus, the fit reported here utilizes double the number of vibrational levels as the THSOF fit, and extends to nearly twice as high of internal energy.

The data included in the fit are listed in Table I. The

TABLE I. Data included in the effective Hamiltonian fit. The data in the second section of the table are 31 pure bending vibrational levels, observed through absorption spectroscopy, that were previously included in the THSOF fit. The first section of the table lists 51 pure bending vibrational levels that were recently assigned by the application of numerical pattern recognition to our dispersed fluorescence data set (see Ref. 2). The columns N_b, l, and g/u specify the polyad assignments of the vibrational levels included in the fit. For the $l=0$ polyads, the parity of the vibrational wave functions is specified as a superscript; that is, ''+'' specifies a vibrational wave function of $\Sigma^+_{g/u}$ symmetry species, and ''−'' specifies $\Sigma^-_{g/u}$.

N_b	l	g/u	E_{obs} (cm^{-1})	E_{calc} (cm^{-1})	N_b	l	g/u	E_{obs} (cm^{-1})	E_{obs} (cm^{-1})
6	$0^+/2$	g	3770.3	3770.1	20	$0^+/2$	g	13 428.7	13 426.4
6	0^+	g	3942.5	3942.6	20	2	g	13 224.7	13 228.1
6	2	g	3949.5	3949.5	20	2	g	13 443.4	13 441.8
8	$0^+/2$	g	5068.8	5070.5	22	0^+	g	14 663.4	14 665.0
8	0^+	g	5216.0	5217.6	22	2	g	14 677.5	14 680.2
8	2	g	5221.0	5223.9	22	$0^+/2$	g	14 736.0	14 736.5
10	$0^+/2$	g	6386.1	6386.4	22	0^+	g	14 755.8	14 757.4
10	$0^+/2$	g	6423.0	6424.3	22	2	g	14 767.5	14 768.8
10	0^+	g	6462.1	6462.4	22	$0^+/2$	g	14 856.2	14 854.2
10	2	g	6511.0	6513.7					
10	0^+	g	6658.5	6660.2	1	1	g	612.9	612.8
10	2	g	6664.5	6667.6	1	1	u	730.3	730.3
12	$0^+/2$	g	7733.6	7731.6	2	0^+	g	1230.4	1230.7
12	2	g	7753.9	7753.8	2	0^+	g	1449.1	1449.1
12	$0^+/2$	g	7773.3	7772.9	2	2	g	1233.5	1233.7
12	0^+	g	7808.5	7806.4	2	2	g	1463.0	1463.0
12	2	g	7814.0	7813.0	2	0^+	u	1328.1	1328.0
12	0^+	g	7836.0	7834.4	2	0^-	u	1340.5	1340.4
12	2	g	7843.0	7841.0	2	2	u	1347.5	1347.5
12	$0^+/2$	g	7951.5	7949.0	3	1	g	1855.7	1856.4
14	0^+	g	9041.0	9040.6	3	1	g	2049.1	2049.0
14	2	g	9046.0	9046.8	3	1	g	2067.0	2066.9
14	$0^+/2$	g	9073.4	9071.1	3	3	g	1861.9	1862.4
14	$0^+/2$	g	9090.3	9091.4	3	3	g	2084.8	2084.8
14	2	g	9102.6	9102.8	3	1	u	1941.2	1941.3
14	0^+	g	9136.2	9135.6	3	1	u	1960.9	1961.1
14	2	g	9143.5	9144.5	3	1	u	2170.3	2170.5
14	$0^+/2$	g	9162.5	9162.6	3	3	u	1972.6	1972.8
14	2	g	9238.0	9236.2	3	3	u	2198.1	2198.2
16	0^+	g	10 374.0	10 376.4	4	0^+	g	2648.0	2648.1
16	$0^+/2$	g	10 474.8	10 471.9	4	0^+	g	2880.2	2880.5
16	$0^+/2$	g	10 492.7	10 489.5	4	0^-	g	2661.2	2661.2
16	2	g	10 549.1	10 548.5	4	2	g	2666.1	2666.3
16	$0^+/2$	g	10 565.0	10 564.1	4	2	g	2894.1	2894.4
16	$0^+/2$	g	10 577.9	10 575.6	4	0^+	u	2560.6	2561.1
18	$0^+/2$	g	11 812.0	11 812.8	4	0^+	u	2757.8	2757.8
18	$0^+/2$	g	11 904.0	11 900.8	4	0^-	u	2583.8	2584.3
20	0^+	g	13 238.9	13 238.5	4	0^-	u	2783.6	2783.7
20	$0^+/2$	g	13 327.3	13 326.7	4	2	u	2561.5	2561.9
20	2	g	13 341.4	13 340.9	4	2	u	2589.7	2590.2
20	2	g	13 356.5	13 359.4	4	2	u	2773.2	2773.1
20	$0^+/2$	g	13 552.9	13 551.1	4	2	u	2795.5	2795.5

column marked l in this table requires explanation. All data that were included in the THSOF fit were $J=0$ internal energies. For the DF data, which do not access $J=0$ rotational levels, these rotationless vibrational energies were *inferred* from the experimental data, by subtracting out the "$2B$ rotational contribution . . . prior to the fit."[10] This approach implicitly assumes that the fractionation pattern for a $(J=0,\ l=0)$ polyad, which is not observed experimentally in the DF spectra, will be identical to that of the corresponding $(J=1,\ l=0)$ polyad that is observed experimentally, after a constant shift of $2B$. This assumption would be rigorously correct in the absence of vibration-rotation coupling; in practice, deviations from this assumption are negligible compared with the uncertainties in the observed transitions, even at 15 000 cm^{-1}.

However, the $(J=1,\ l=0)$ lines are only one of two sets of rotational lines that are observed in the DF spectra, the other set being $(J=2,\ l=2)$. Unfortunately, it *cannot* be assumed that the fractionation patterns for the $(J=2,\ l=2)$ polyads are the same, except for a constant shift, as the unobserved $(J=0,\ l=0)$ polyads, because the $l=2$ polyads do not contain the same number of states as the corresponding $l=0$ polyads. In the THSOF fit, the $(J=2,\ l=2)$ lines could be safely ignored, because it can be demonstrated that, at low internal energy, these lines tend to be nearly perfectly blended with corresponding $(J=1,\ l=0)$ lines due to a coincidence arising from the signs and magnitudes of the g_{44} and B parameters.[1] At higher internal energy, the situation is rather different. Although some pairs of $(J=1,\ l=0)$ and $(J=2,\ l=2)$ levels can be observed, see Fig. 2, they tend to be resolvable at the experimental resolution. Throwing out the observed $(J=2,\ l=2)$ lines at high internal energy would result in a loss of information that is valuable from the standpoint of fitting the desired parameters.

Therefore, in order to include observed $(J=2,\ l=2)$ lines in the fit, we have chosen not to attempt to infer the energies of the rotationless vibrational levels from the data, but instead have fit the *ro*vibrational energies that can be determined directly from the data. In a technical sense, this implies that for each pure bending polyad observed experimentally, two matrices were diagonalized in the fit, one for $(J=2,\ l=2)$ and one for $(J=1,\ l=0)$. The rotational energies of the zero-order states were calculated using

$$E_{\mathrm{rot}}=B_vJ(J+1),$$

$$B_v=B_0-\sum_{k=1}^{5}\alpha_kv_k,$$

and the values of the rotational parameters were constrained to those listed in Table V of Ref. 11. For those observed transitions which did correspond to an unresolvable pair of $(J=2,\ l=2)$ and $(J=1,\ l=0)$ levels, marked "$0^+/2$" in the table, the two corresponding calculated eigenenergies were averaged to estimate the approximate location of the maximum of the peak that would be observed experimentally.

TABLE II. Parameters determined from least-squares fit of the pure bending effective Hamiltonian to the data set described in the text. Numbers in parentheses are 2σ uncertainties in the last digit. All parameters are in units of cm^{-1}.

ω_4	608.656 (34)
ω_5	729.137 (38)
x_{44}	3.483 (13)
x_{45}	−2.256 (28)
x_{55}	−2.389 (14)
g_{44}	0.676 (22)
g_{45}	6.671 (30)
g_{55}	3.535 (20)
y_{444}	−0.030 60 (72)
y_{445}	0.0241 (48)
y_{455}	0.0072 (52)
y_{555}	0.009 54 (84)
$\mathring{r}_{45}$	−6.193 (32)
r_{445}	0.0303 (48)
r_{545}	0.0109 (64)
s_{45}	−8.572 (52)

The new fit also differs from the previous fit in several other technical details. First, two new parameters were included: y_{445} and y_{555} (the previous fit had included only y_{444} and y_{455}). The effective Hamiltonian used here therefore includes the diagonal elements,

$$\begin{aligned}\langle v_4^{l_4},v_5^{l_5}|H^{eff}|v_4^{l_4},v_5^{l_5}\rangle &=\omega_4v_4+\omega_5v_5+x_{44}v_4^2+x_{45}v_4v_5+x_{55}v_5^2\\ &\quad+y_{444}v_4^3+y_{445}v_4^2v_5+y_{455}v_4v_5^2+y_{555}v_5^3\\ &\quad+g_{44}l_4^2+g_{45}l_4l_5+g_{55}l_5^2,\end{aligned}$$

and the following off-diagonal elements (and their Hermitian conjugates),

(a) Darling-Dennison Bend I

$$\langle v_4^{l_4},v_5^{l_5}|H^{eff}|(v_4-2)^{l_4},(v_5+2)^{l_5}\rangle=\frac{s_{45}}{4}[(v_4^2-l_4^2)(v_5+l_5+2)(v_5-l_5+2)]^{1/2},$$

(b) Darling-Dennison Bend II

$$\begin{aligned}\langle v_4^{l_4},v_5^{l_5}|H^{\mathrm{eff}}|(v_4-2)^{l_4\mp2},(v_5+2)^{l_5\pm2}\rangle &=\frac{r_{45}+2g_{45}}{16}[(v_4\pm l_4)(v_4\pm l_4-2)(v_5\pm l_5+2)\\ &\quad\times(v_5\pm l_5+4)]^{1/2},\end{aligned}$$

(c) vibrational l-doubling

$$\langle v_4^{l_4},v_5^{l_5}|H^{\mathrm{eff}}|v_4^{l_4\pm2},v_5^{l_5\mp2}\rangle=\frac{r_{45}}{4}[(v_4\mp l_4)(v_4\pm l_4+2)(v_5\pm l_5)(v_5\mp l_5+2)]^{1/2},$$

in which

$$r_{45}=\mathring{r}_{45}+r_{445}(v_4-1)+r_{545}(v_5-1).$$

A second technical detail is that the infrared absorption data were weighted more strongly in the fit than the DF data, both because the absorption data are calibrated to higher accuracy than the DF data (<0.01 vs $\sim2\ \mathrm{cm}^{-1}$), and because the DF data span a range of internal energy that extends to much higher $E_{\rm vib}$ than the absorption data. At higher internal energy, it is more likely that small, random perturbations that are not accounted for by the model will be present. The ratio of weights used in the fit was 25:1 (absorption:DF); other ratios were tested but resulted in little change in the fitted parameters. This weighting differs considerably from the reciprocal squared uncertainty, but we believe this choice of relative weights to be justified physically, if not statistically.

The methodology of the fit also had to be modified in order to meet certain challenges that are inherent in fitting data at internal energy as high as 15 000 $\rm cm^{-1}$. First, at the outset of the fit, at high internal energy (e.g., $N_b=22$) it was not obvious which calculated eigenstates corresponded to which observed transitions [see Fig. 2(b)]. For this reason, the fit had to be performed in a bootstrapping fashion, by first refining the quality of the fit below 10 000 $\rm cm^{-1}$, and then gradually adding in eigenenergies above 10 000 $\rm cm^{-1}$, until the correspondence between the observed and calculated eigenenergies became obvious up to 15 000 $\rm cm^{-1}$. At this point, all intense, sharp peaks in the DF spectra were included in the fit.

Even when the correspondence between observed transitions and calculated eigenstates is obvious by eye, it is not always trivial to establish this correspondence numerically. Generally, only a small fraction of the eigenstates within a given polyad are observable within the signal-to-noise of the experiment, and the fitting routine must decide in an automated fashion which calculated eigenstate corresponds to which observed transition in order to calculate the (chi squared) merit function. When the correspondence is obvious visually, it is usually because *both* the frequency *and* the intensity of the calculated transition match well with those of the observed line, and we have encoded this criterion numerically by defining a metric, $M_{c,o}$, which quantifies how well a calculated eigenstate c and an observed transition o match each other,

$$M_{c,o}=M^E_{c,o}M^I_{c,o},$$

$$M^E_{c,o}=\exp\left\{-\frac{(E_c-E_o)^2}{2(\Delta E)^2}\right\},$$

$$M^I_{c,o}=\exp\left\{-\frac{[(I_c-I_o)/(I_c+I_o)]^2}{2(\Delta I)^2}\right\}.$$

This metric is defined to be the product of two factors, $M^E_{c,o}$ and $M^I_{c,o}$, which quantify the frequency and intensity match, respectively. Each of these factors are defined as Gaussian functions of the discrepancy between the observed and calculated quantities, such that the metric $M_{c,o}$ can only attain a value near 1.0 if *both* the frequencies *and* intensities match well. The quantities ΔE and ΔI define what is meant by ‘‘a good match’’ for the frequencies and intensities, respectively. For our fits, we chose $\Delta E=5\ \rm cm^{-1}$ and $\Delta I=0.2$. Each time that the merit function was calculated during the fit (which utilized a modified version of the Numerical Recipes[13] Levenberg-Marquardt algorithm), the value of the metric $M_{c,o}$ was calculated for each observed transition that was included in the fit, o, with every calculated eigenstate, c. The calculated eigenstate with the largest value of the metric $M_{c,o}$ with a given observed transition was assumed to be the correct match, and was used to calculate the merit function.

The final parameters that were obtained from this fit are listed in Table II, along with estimated uncertainties in the parameters that were determined from the covariance matrix. This set of parameters reproduces the 84 eigenenergies included in the fit to $\pm 1.4\ \rm cm^{-1}$ (1σ). All of the parameters have been determined to greater precision than in the THSOF fit, but most of the parameters have not changed by much more than the 2σ error that was reported in the THSOF fit. The exceptions are x_{44}, y_{455}, $\mathring{r}_{45}$, and r_{545}, which were previously reported as 3.600, 0.093, −5.942, and −0.167 $\rm cm^{-1}$, respectively (the new values are 3.483, 0.0242, −6.193, and 0.0110). The likely reason that the first two of these parameters changed by substantial amounts is that the THSOF fit imposed the constraint that $y_{445}=y_{555}=0.0$. The $\mathring{r}_{45}$ and r_{545} parameters are much better determined in the current fit due to the inclusion of states at high internal energy ($\sim$15 000 $\rm cm^{-1}$) which are coupled very strongly by the Darling-Dennison resonances that are parameterized by the $\mathring{r}_{45}$ and r_{545} constants. However, despite the fact that most of the parameters have not changed by large amounts relative to the THSOF fit, the improvement in the qualitative agreement between the calculated and observed spectrum in Fig. 2 is quite dramatic at 15 000 and even at 9000 $\rm cm^{-1}$.

It is worth reiterating that our development of an $H^{\rm eff}$ with predictive power up to 15 000 $\rm cm^{-1}$ is only possible because we have been able to extract single fractionated bright states from our DF data set using numerical pattern recognition, even though severe, systematic overlap exists between the fractionated patterns associated with several bright states. This numerical procedure would have been infeasible if the polyad quantum numbers were not at least approximately conserved; the ability to model quantitatively the extracted patterns provides even stronger evidence that the short-time dynamics of acetylene can be efficiently described in terms of these polyad numbers. Further, for the pure bending polyads, only a small number of resonances (Darling-Dennison and vibrational l-resonance) are necessary in order to accurately describe the short-time (∼1 ps) dynamics. In the remainder of this paper we explore the insights into the short-time bending dynamics of acetylene that this $H^{\rm eff}$ permits.

IV. TIME-DOMAIN DYNAMICS

The bright states that are accessed experimentally are not eigenstates of the $H^{\rm eff}$. In the frequency domain, this fact is manifested by a fractionation of the bright state. In the time domain, the bright state is not stationary, and its time-evolution is governed by

$$\Psi(t)=\sum_{j=1}^{N} c_j\psi_j e^{-i\omega_j t},$$

in which ψ_j are the eigenstates and ω_j are the corresponding frequencies $(E_j/\hbar)$, $\Psi(0)$ is the bright state, c_j

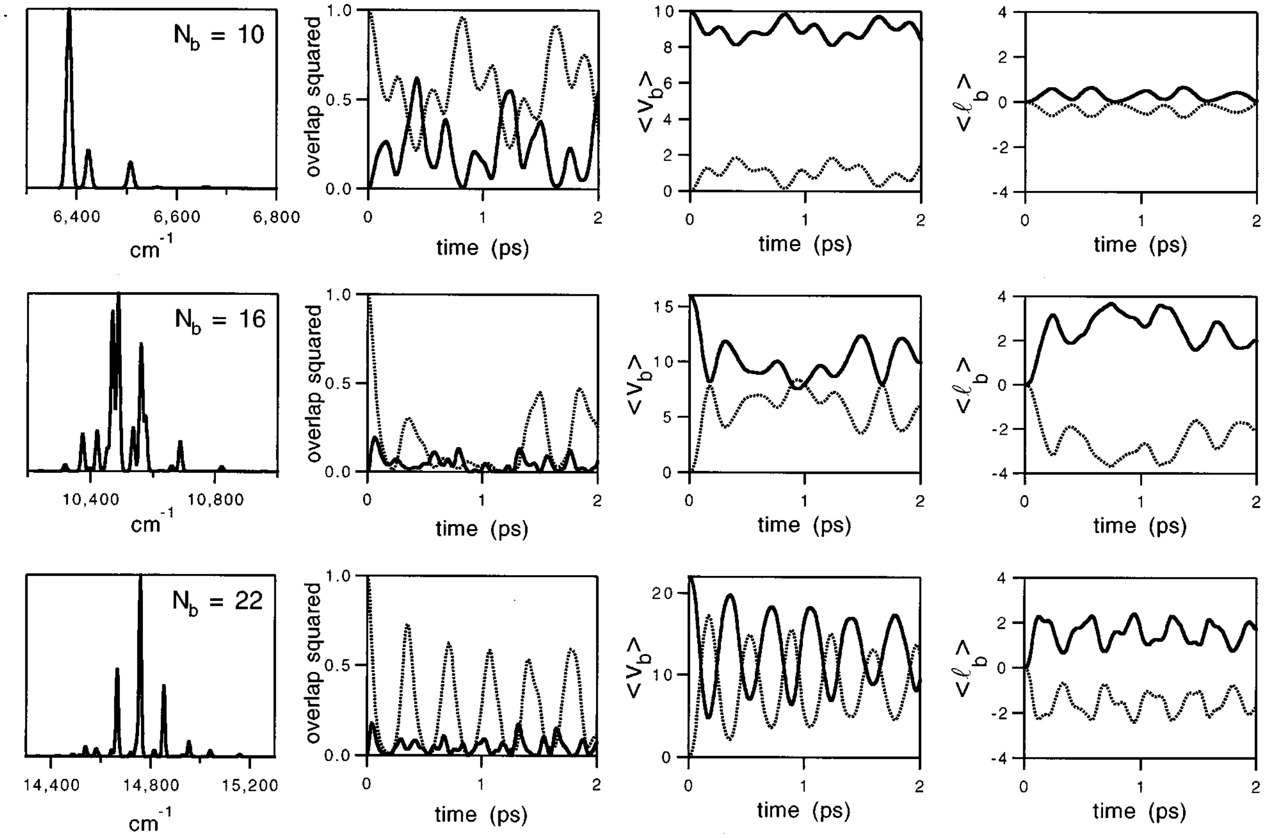

FIG. 3. Predictions of the H^{eff} for three pure bending polyads, $N_b=10,16,22$, $l=0$. Column 1: fractionation patterns of the bright state, $(0,0,0,v_4{}^0,0^0)$ in each polyad. Column 2: survival probability for the bright state, over the first 2.0 ps (dotted line) and time-dependent projection squared of the wave packet onto one of the two gateway states $(0,0,0,(v_4-2)^0,2^0)$ (solid line). Column 3: average number of quanta (v_4,v_5) in the *trans* (solid line) and *cis* bend (dotted line) modes as a function of time. Column 4: average number of quanta of vibrational angular momentum (l_4,l_5) in the two bending modes as a function of time. The IVR appears to grow more complicated from $N_b=10$ to $N_b=16$, but the curiously simple fractionation pattern and survival probability for $N_b=22$ is surprising.

$=\langle\Psi(0)|\psi_j\rangle$, and N is the number of states within the relevant polyad. The coefficients c_j are known from the unitary transformation that diagonalizes the H^{eff}, and thus the time-evolution of the initially prepared bright state is completely determined from information obtainable from the frequency domain spectrum.

The survival probability of the initially prepared state, $|\langle\Psi(0)|\Psi(t)\rangle|^2$, is frequently used to represent this dynamics, and we present in the second column (dotted lines) of Fig. 3 the survival probabilities for the bright states $(l=0)$ with 10, 16, and 22 quanta of *trans* bending excitation. For comparison, the fractionation patterns of the bright states (as predicted by the H^{eff}) are also depicted in the first column of this figure (note that the linewidth has been added only for ease of viewing). These two representations of the dynamics, of course, have the same information content; however, they can be considered to be complementary in terms of *conceptualization* of the dynamics.

The survival probability does not, however, provide a complete picture of the dynamics, in the sense that when the survival probability is low, the overlap of the wave packet with other zero-order states must be large . . . but which zero-order states? One could, of course, calculate the overlap of the time-evolving wave packet with any of the zero-order states in the relevant polyad, but for the $N_b=22$ polyad, for example, the total number of zero-order states is 42, and it is not practical to plot the overlap of the wave packet with *each* of these states. For this reason, we have plotted only one such trace in the second column, which is the overlap squared of the time-evolving wave packet with the zero-order state $(0,0,0,(N_b-2)^0,2^0)$ (solid line). This zero-order state is chosen because it is one of only two states within any pure bending polyad that is coupled directly with the bright state $(0,0,0,N_b^0,0^0)$ by the known anharmonic resonances. In particular, the state that we have chosen couples to the bright states *via* the Darling-Dennison I resonance; the other state that couples directly to the bright state is $(0,0,0,(N_b-2)^{+2},2^{-2})$, *via* the Darling-Dennison II resonance. We refer to these two states as *gateway* states because, in order for the vibrational excitation to flow from the bright state into the remainder of the polyad, it must first flow through the $(0,0,0,(N_b-2)^0,2^0)$ and $(0,0,0,(N_b-2)^{+2},2^{-2})$ states.

To complement the time-dependent overlap of the wave packet with the bright state and one of the two gateway states, we also present in the third and fourth columns two other time-domain representations of the dynamics, which are the time evolutions of the expectation values of the number operators, $\hat{v}_4$, $\hat{v}_5$, $\hat{l}_4$, and $\hat{l}_5$,

$$\langle v_b(t)\rangle = \langle \Psi(t)|\hat{v}_b|\Psi(t)\rangle,$$

$$\langle l_b(t)\rangle = \langle \Psi(t)|\hat{l}_b|\Psi(t)\rangle, b=4,5.$$

In colloquial terms, $\langle v_4(t)\rangle$ and $\langle v_5(t)\rangle$ represent the average number of quanta in the *trans* and *cis* bending modes, respectively, as a function of time, and $\langle l_4(t)\rangle$ and $\langle l_5(t)\rangle$ are the average number of quanta of vibrational angular momentum in the two bending modes as a function of time. Thus, in the absence of plots of the overlap of the wave packet with every one of the relevant zero-order states, these time-dependent expectation values provide some insight into the dynamics of the wave packet within the interior of the polyad, which is comprised of zero-order states that are not directly coupled to the bright state. Note that $\langle v_4(0)\rangle = N_b$, $\langle v_5(0)\rangle = \langle l_4(0)\rangle = \langle l_5(0)\rangle = 0$, and that $\langle v_4(t)\rangle + \langle v_5(t)\rangle = N_b$ and $\langle l_4(t)\rangle + \langle l_5(t)\rangle = l$ for all time. The signs of $\langle l_4(t)\rangle$ and $\langle l_5(t)\rangle$ are arbitrary.

We now consider the specific insights that this figure provides into the dynamics associated with the $N_b=10$, 16, and 22 bright states. Both the frequency and time-domain representations of the IVR associated with the $(0,0,0,10^0,0^0)$ bright state emphasize the relative simplicity of the dynamics at low internal energy ($\sim$6000 cm^{-1}). The fractionation pattern contains predominantly one main peak and two smaller peaks at higher internal energy which might be described as perturbers of the bright state (note that one of these two smaller peaks is blended and represents two eigenstate transitions). Together, these four eigenstates account for nearly 99% of the bright state character (the most intense peak accounts for 72.7%). In the time domain, the survival probability of the bright state displays a multiple quantum beating pattern, which also underscores the small number of levels involved in the dynamics. The survival probability never falls below 20%, at least not during the first 2.0 ps. The overlap of the wave packet with the gateway state $(0,0,0,8^0,2^0)$ nearly mirrors the survival probability, indicating that much of the dynamics of the wave packet is accounted for by transfer of the vibrational excitation between the bright state and the gateway states. The wave packet never substantially populates the interior of the polyad, as seen in the plots of $\langle v_b(t)\rangle$ and $\langle l_b(t)\rangle$; during the first 2.0 ps of the dynamics, only about two quanta of the *trans* bend excitation are exchanged for *cis* bending excitation, indicating that the wave packet evolution tends not to proceed beyond the gateway states.

At $N_b=16$, the dynamics is strikingly different. The fractionation pattern for the bright state with $v_4=16$ is very complicated; the eigenstate with maximal intensity accounts for only 24.6% of the bright state character. In the time domain, the survival probability of the bright state displays a fast early time decay followed by a series of irregular partial recurrences. The 1/*e* time (τ) for the initial decay is $\sim$80 fs, and by 220 fs, the survival probability reaches a minimum value of less than 0.02. The overlap of the wave packet with the gateway state in this case does not even approximately mirror the survival probability, which indicates that the wave packet passes through the gateway state and into the interior of the polyad. As a result, the *trans* and *cis* bend degrees of freedom exchange substantial vibrational excitation as well as angular momentum, as seen in the plots of $\langle v_b(t)\rangle$ and $\langle l_b(t)\rangle$. Thus, both the time and frequency domain pictures indicate a drastic change in the nature and extent of the IVR from 6000 to 10 000 cm^{-1}. Of course, the two intervening pure bending polyads (N_b=12,14) have been omitted from Fig. 3, and the change in the qualitative behavior is gradual from $N_b=10$ to $N_b=16$.

TABLE III. Dilution factors (y) calculated for several classes of bright states. Note that $l=0$ refers to the ($J=1$, $l=0$, e parity) lines observed experimentally, and $l=2$ refers to ($J=2$, $l=2$, f parity). The columns labeled N list the total number of states within the relevant polyads, for reference.

N_b	y ($l=0$)	N ($l=0$)	y ($l=2$)	N ($l=2$)
4	0.98	4	0.99	4
6	0.95	6	0.95	8
8	0.85	9	0.86	12
10	0.56	12	0.58	18
12	0.36	16	0.31	24
14	0.22	20	0.13	32
16	0.16	25	0.10	40
18	0.22	30	0.17	50
20	0.30	36	0.11	60
22	0.24	42	0.11	72

This qualitative change in behavior would *seem* to be accounted for trivially in terms of the increase in the number of states in each polyad and the strength of the matrix elements that couple them. However, the frequency and time-domain dynamics for the $N_b=22$ bright state indicate that such an argument is overly simplistic. From N_b=16 to N_b=22, the size of the polyads continues to grow as well as the magnitudes of the off-diagonal matrix elements, but the fractionation pattern and survival probability for the N_b=22 bright state actually appear to be *less* complicated than those for the N_b=16 bright state. A total of only three eigenstates account for 72.0% of the bright state character; the most intense peak accounts for 43.3%. Although the early time decay in the survival probability for $(0,0,0,22^0,0^0)$ is somewhat faster ($\tau\approx60$ ps) than that for the $(0,0,0,16^0,0^0)$ ($\tau\approx80$ ps), the $(0,0,0,22^0,0^0)$ survival probability displays a series of strikingly regular, and strong ($>$50%), partial recurrences. On the other hand, the overlap of the wave packet with the gateway state, $(0,0,0,20^0,2^0)$, looks at least as complicated as the corresponding trace for N_b=16. The regular series of recurrences in the survival probability is not, therefore, due to simple quantum beating between the bright state and the gateway states. Rather, the recurrences are mirrored in the strong oscillations of $\langle v_b(t)\rangle$, and to a lesser extent, $\langle l_b(t)\rangle$, indicating that some regularity is preserved in the dynamics despite the fact that the wave packet penetrates deeply into the interior of the polyad.

Taken together, the plots in Fig. 3 indicate that the extent and complexity of IVR for the *trans* bending bright states in the pure bending polyads is not a simple function of internal energy. Without a conceptual framework for understanding the unexpectedly complicated trends in the IVR, the dynamics in the $N_b = 22$ polyad seems mysterious, being both extensive (deep penetration into the interior of the polyad) and simple (strong, regular recurrences; simple fractionation pattern). In Sec. VI, a conceptual framework will be presented which explains all of the qualitative trends observed here. First, however, we consider a quantitative measure of the extent of IVR, the dilution factor, which provides further insights into the trends in IVR as a function of internal energy.

V. DILUTION FACTORS

The dilution factor, or inverse participation ratio,[14] is frequently employed as a numerical measure of the fractionation of a zero-order state.[15,16] Dilution factors are usually reported for the experimentally accessible bright states, but if an adequate model is available to predict the fractionation patterns of zero-order states that have not been observed experimentally, then dilution factors can be calculated for these ''hypothetical bright states'' as well.[17–19] In the context of the pure bending H^{eff}, the dilution factor y is defined as

$$y_k = \sum_{j=1}^{N} |c_{jk}|^4,$$

in which k represents a particular zero-order state, j is an index over eigenstates, N is the number of eigenstates within the polyad that contain the zero-order state, and c_{jk} is the projection of the eigenstate onto the zero-order state (one element of the eigenvector matrix). Note that $1 \geqslant y \geqslant 1/N$; bright states that display little fractionation have dilution factors near unity, whereas bright states that display extensive fractionation may have dilution factors that approach $1/N$.

It should be noted that generalizations of the dilution factor have been introduced in the literature, the most prominent of which is the $P(a|b)$ statistic, which was introduced by Nordholm and Rice[20] and has been used in many theoretical treatments by Heller.[21–23] This statistic is defined as

$$P(a|b) = \sum_{j=1}^{N} |c_{ja}|^2 |c_{jb}|^2.$$

Note that for $a = b$, the definition reduces to that for the dilution factor; thus, the dilution factor can be considered a special case of the $P(a|b)$ statistic. For $a \neq b$, the statistic describes energy flow between two zero-order states. An analog of the dilution factor which is eigenstate specific, as opposed to zero-order state specific, has also been reported;[23] this statistic provides a measure of the inverse of the number of zero-order states with which a particular eigenstate has substantial overlap. These generalizations of the dilution factor, although extremely useful in general, will not be considered further in this work because they are not as directly relevant to an explanation of the unusual dynamics described in the preceding section.

Table III lists the dilution factors for the pure bending bright states that are observed experimentally. Note that the dilution factors for $l = 0$ and $l = 2$ are nearly identical up to $N_b = 10$, but that at higher internal energy the dilution factors for the $l = 2$ bright states are substantially smaller (indicating greater fractionation) than those for the corresponding $l = 0$ bright states. This is another manifestation of the observation made in Sec. II that, above $\sim 8000\ \mathrm{cm}^{-1}$, $(J = 1,\ l = 0)$ and $(J = 2,\ l = 2)$ rotational lines show a diminished tendency to occur in nearly degenerate pairs. The fundamental reason for the dissimilarity of the $l = 0$ and $l = 2$ dilution factors is that the $l = 2$ polyads contain more states than the corresponding $l = 0$ polyads. At low internal energy, where the dynamics is restricted and tends not to sample the interior of the polyad, the total number of states in the polyad is largely irrelevant. However, at higher internal energy, where the dynamics samples many of the states in the polyad, the larger $l = 2$ polyads display more complicated dynamics than those with $l = 0$.

The other striking aspect of this table is that the dilution factors for both the $l = 0$ and $l = 2$ bright states do not decrease monotonically with increasing internal energy. Rather, in both cases, the absolute minimum in the dilution factors occurs at $N_b = 16$, which lies at only $10\,500\ \mathrm{cm}^{-1}$. Note that this counterintuitive trend, in which the dilution factors decrease monotonically up to $N_b = 16$, then increase somewhat before decreasing again, is not obvious simply by inspecting the fractionated bright state patterns in Fig. 1. Direct interpretation of the fractionation patterns is complicated by the presence of two rotational lines, $(J = 1,\ l = 0)$ and $(J = 2,\ l = 2)$, in the spectra, which do not appear in nearly degenerate pairs at higher internal energy. The splitting of these pairs of rotational states gives the *appearance* of more substantial fractionation at higher internal energy, and in the absence of an accurate H^{eff}, one might conclude, incorrectly, that fractionation increases more or less monotonically with internal energy.

These trends in the dilution factors, of course, confirm the qualitative observations that were made on the time-domain dynamics in the preceding section, namely, that the dynamics of the $(0,0,0,22^0,0^0)$ bright state seemed simpler in certain senses than that of $(0,0,0,16^0,0^0)$, which lies $>4000\ \mathrm{cm}^{-1}$ lower in internal energy. One might wonder whether this unusual trend in the dynamics is unique to the set of bright states that are accessible experimentally from the $\tilde{A}$ state of acetylene, or whether the overall structure of the polyads changes in an unusual fashion, which might imply that the dynamics for other classes of bright states would change in an unusual manner as well. In other words, how typical are the dynamics of the pure *trans* bending bright states relative to other bright states that we can *imagine* accessing (even if such access might be difficult or impossible experimentally)?

Figure 4 attempts to address this question by plotting the distribution of dilution factors for all of the zero-order states in the $N_b = 10,16,22$, $l = 0$ polyads. The $N_b = 10$ polyad, for instance, encompasses a total of 12 zero-order states. The experimentally accessible bright state in this polyad, $(0,0,0,10^0,0^0)$, has the second highest dilution factor among all of the zero-order states. The only zero-order state with a larger dilution factor is $(0,0,0,0^0,10^0)$. In other words, if it were possible to excite pure *cis* bending, as opposed to pure *trans* bending, bright states experimentally, then the fractionation pattern that would be observed for the $N_b = 10$ polyad would be slightly simpler. Excitation of any other class of

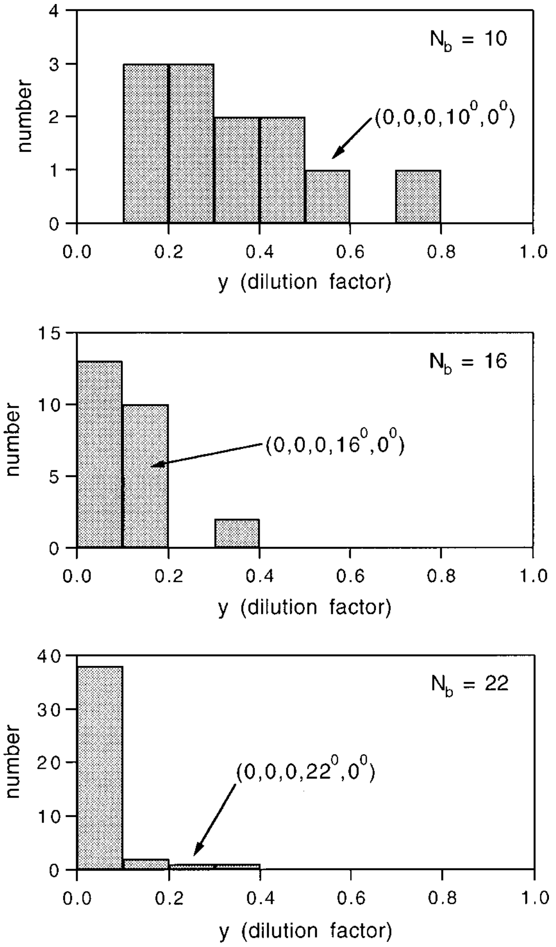

FIG. 4. Histograms representing the distribution of dilution factors for all zero-order states that compose a polyad. The bright states accessed experimentally generally have dilution factors that are among the highest (least fractionated) within the polyad.

zero-order states, which would necessarily involve both *trans* and *cis* bending, would result in a more complicated fractionation pattern. In this sense, then, the dynamics of the bright state that is accessed experimentally cannot be considered to be typical of the dynamics that would be observed for most other conceivable classes of bright states.

The observation that $(0,0,0,0^0,10^0)$ and $(0,0,0,10^0,0^0)$ possess the largest dilution factors in the $N_b=10$ polyad is consistent with studies of many molecular systems which have found that zero-order states with all of the vibrational excitation residing in just one of the modes tend to have fractionation patterns that are atypically simple.[24,25] These experimental observations have been explained using the theoretical constructs of ''exterior'' and ''interior'' states, and the rather similar concept of ''extreme motion states.''[26,27] The concept of exterior states is associated with a phenomenological argument that states with excitation localized primarily in one mode (or, in the case of larger molecules, in a small number of modes) of the molecule tend be coupled to fewer other zero-order states *via* the important anharmonic resonances than do states with vibrational excitation which is spread more evenly among the modes. It was noted in the preceding section, for instance, that the bright states $(0,0,0,v_4{}^0,0^0)$ are coupled to only two gateway states, $(0,0,0,(v_4-2)^{+2},2^{-2})$ and $(0,0,0,(v_4-2)^0,2^0)$. The concept of extreme motion states provides a theoretical foundation for these arguments, the central tenet of which is an adiabatic decoupling of the extreme motion (exterior) states from other states. It should be noted that certain limitations of the concept of extreme motion states have been pointed out by Lehmann, Scoles, and coworkers, on the basis of their work on propyne.[28] Namely, they note that if the vibrational energy of a molecule is delocalized over modes that interact only weakly with each other, then the excitation in each mode can be expected to relax independently; in other words, an increase in the delocalization of vibrational excitation can, in certain cases, result in a *decrease* in the rate of IVR. However, these criticisms of the concept of extreme motion states are relevant primarily to molecules much larger than acetylene.

On the whole, the concept of extreme motion (exterior) states appears to be profitable for the pure bending polyads of acetylene. The states with all of the vibrational excitation localized in the *cis* bending mode *always* have the largest dilution factor in a given pure bending polyad (at least up to $N_b=22$). In the $N_b=10$ and $N_b=22$ polyads, which are illustrated in Fig. 4, the bright state, which has all of the vibrational excitation in *trans* bend, has the second highest dilution factor. In $N_b=16$, however, the *trans* bend bright state has only the fourth highest dilution factor, and nine other zero-order states have dilution factors that also range between 0.1 and 0.2. In other words, in $N_b=16$, the bright state does not behave like an exterior state, in the sense that its IVR seems to be somewhat more typical of the totality of zero-order states within the polyad. From this perspective, then, the unusual trends in IVR that were examined in the preceding section reflect the way in which the bright state behaves like an exterior (extreme motion) state at low ($N_b=10$) and high ($N_b=22$) internal energy, but not at intermediate ($N_b=16$) energy. We provide a framework for understanding this behavior of the bright state in the next section.

VI. ZERO-ORDER ENERGIES AS A FRAMEWORK FOR UNDERSTANDING TRENDS IN DYNAMICS

The unexpectedly complicated trends in IVR above 10 000 cm^{-1} that were noted in the two preceding sections

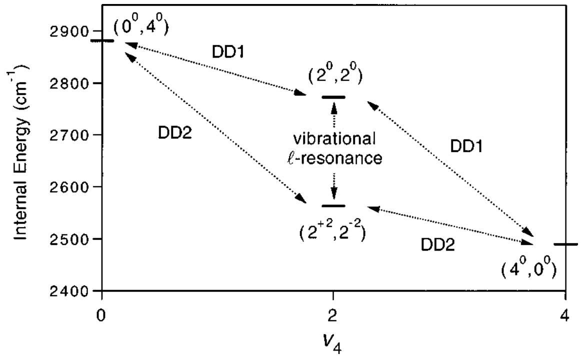

FIG. 5. Graphical depiction of the zero-order energies within a pure bending polyad ($N_b=4$) which elucidates the resonance structure. The zero-order states are arranged in stacks according to v_4, with the top state in each stack having $l_4=0$, and each successively lower state having l_4 increased by 2. Note that the energy separation between the $(2^0,2^0)$ and $(2^{+2},2^{-2})$ states has been exaggerated for purposes of illustration.

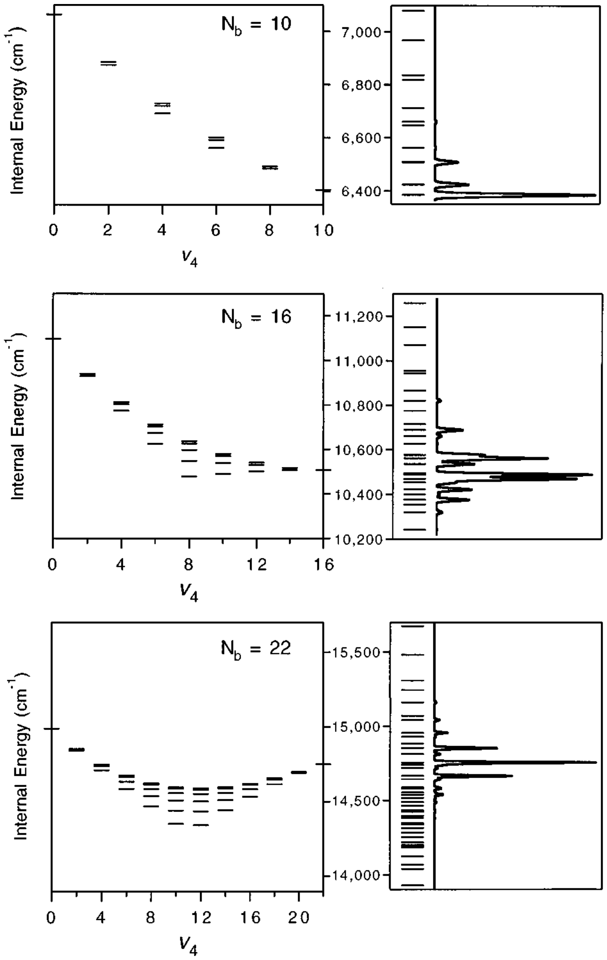

FIG. 6. Left column: Energies of the zero-order states within the $N_b = 10$, 16, and 22 polyads, plotted as a function of v_4. The arrangement of the states is explained in Fig. 5. Right column: eigenenergies of the polyads (horizontal lines) as well as the simulated spectrum (solid line). The energy arrangement of the zero-order states provides insight into the complicated trends in IVR observed in Fig. 3.

can be understood by investigation of the structure of the blocks of the H^{eff} matrix that correspond to each of the relevant polyads. It should be noted at the outset that the structure of the polyad blocks of the H^{eff} at high internal energy is rather complicated, in the sense that any given zero-order state typically interacts with several other states *via* the known anharmonic resonances. In addition, many off-diagonal matrix elements have magnitudes that are substantially larger than the energy differences between the zero-order states that they couple.

However, we have found that an investigation of the zero-order energies of the states within a polyad provides a compact framework for understanding certain key elements of the dynamics. The zero-order energies are the diagonal elements of the H^{eff}; they can be considered to represent the energies of the states within a polyad if one could turn off the resonances. Thus, without considering the details of the resonances that couple the zero-order states, the zero-order energies allow one to identify pairs or groups of zero-order states that have small energy differences, and thus might be expected to interact strongly due to small energy denominators.

Rather than simply list the zero-order energies for states within a polyad, however, one can gain greater insight into the structure of the H^{eff} by plotting the zero-order energies in a manner related to the resonance structure that couples the zero-order states. In Fig. 5 we illustrate one such way of organizing the zero-order energies, according to the quantum numbers of the corresponding zero-order states, (v_4, l_4, v_5, l_5). For each polyad, $N_b = v_4 + v_5$, so either v_4 or v_5 needs to be specified, but not both. In addition, we focus on the $l=0$ polyads, such that $l_4 = -l_5$. Therefore, a pair of quantum numbers, such as $(v_4, |l_4|)$, is sufficient to label each zero-order state. In Figs. 5 and 6, the v_4 quantum number is labeled along the x-axis of the zero-order energy plots, and in each stack of zero-order states at the same value of v_4, the highest energy state corresponds to $|l_4| = 0$, and each successively lower state has a value of $|l_4|$ that is two greater than that of the preceding state. The stacks contain the largest number of states at intermediate values of v_4 due to the constraint that $|l_4| \leq \min(v_4, v_5)$.

This organization of the zero-order energies is convenient, because the anharmonic resonances in the H^{eff} can be illustrated graphically in a simple fashion. For instance, the l-doubling resonance, which exchanges two quanta of l_4 for two quanta of l_5 without changing v_4 or v_5, couples only zero-order states that are in the same v_4 stack on the diagram. More specifically, a chain of these resonances couples each zero-order state within a stack to the state directly above it and the state directly below it. The two Darling-Dennison resonances, which interchange two quanta between v_4 and v_5, couple states in adjacent v_4 stacks. The Darling-Dennison I resonance, which preserves the values of l_4 and l_5, couples pairs of states in adjacent stacks with the same rank; i.e., the two top states in adjacent stacks, or a pair of states which are each third from the top in adjacent stacks. The Darling-Dennison II resonance, which interchanges two quanta between l_4 and l_5, couples states in adjacent stacks with rank differing by one; i.e., the top state in one stack with the next-to-highest state in an adjacent stack.

In Fig. 6, it can be seen that for $N_b = 10$ (and all lower pure bending polyads), the pure *trans* bending zero-order state (the bright state) has the lowest zero-order energy of all of the states within the polyad. The pure *cis* bending state has the highest zero-order energy, and the states with intermediate values of v_4 and v_5 vary monotonically between these two extremes. This simple structure of the zero-order energies in the low-lying pure bending polyads arises simply from the fact that $\omega_4 < \omega_5$. The resonances that couple the zero-order states at $\sim 6500\ \text{cm}^{-1}$ are relatively weak, and the fractionation pattern observed in the eigenstate spectrum (top right panel) is correspondingly simple. The intense peak below $6400\ \text{cm}^{-1}$ can be labeled as the perturbed bright state (its overlap squared with the zero-order bright state is 0.728), and the two moderately intense peaks at slightly higher internal energy can be identified as the (Darling-Dennison) perturbers.

The zero-order energy diagram for $N_b = 16$ differs from that of $N_b = 10$ in subtle but important ways. First, the bright state is now *nearly*, but not quite, the lowest energy zero-order state within the polyad (the pure *cis* bending state re-

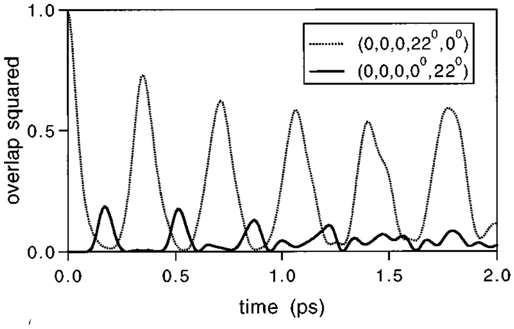

FIG. 7. Time-dependent overlap squared of the $(0,0,0,22^0,0^0)$ bright state wave packet with the pure *trans* bend (dashed line) and pure *cis* bend (solid line) ends of the polyad.

mains at the top). The lowest energy zero-order state is, in fact, $(8^8,8^{-8})$, and a total of 12 zero-order states lie within ± 100 cm^{-1} of the bright state. This proliferation of near-degeneracies among the zero-order states near the bottom of the polyad, coupled with the increase in the magnitude of the matrix elements from $N_b=10$ to $N_b=16$, can be considered to be responsible for the complicated IVR that we noted for this polyad in the preceding two sections. The bright state lies right in the middle of a conglomeration of nearly degenerate, strongly coupled states, leading to a complicated fractionation pattern and time-domain dynamics which are atypical for an exterior state.

The underlying reason for the change in structure in the zero-order energy diagram from $N_b=10$ to $N_b=16$ can be better understood by examination of the zero-order energy diagram for $N_b=22$. The bright state in this case is no longer at the bottom of the polyad; in fact, it has the fourth highest zero-order energy, and lies less than 250 cm^{-1} lower in energy than the pure *cis* bending zero-order state. This fundamental change in the structure of the polyad is due to the fact that the x_{44} and x_{55} anharmonicity constants have opposite signs. In colloquial terms, the opposing anharmonicities give the *trans* bend end of the polyad a chance to catch up to the *cis* bend end at high internal energy. The states in the interior of the polyad, which have $v_4 \approx v_5$, sag down because the cross-anharmonicity between the two modes, x_{45}, is negative.

The zero-order energy diagram for $N_b=22$ helps to explain why the fractionation pattern of $(0,0,0,22^0,0^0)$ appeared to be somewhat less complicated than that of $(0,0,0,16^0,0^0)$. Although the off-diagonal matrix elements, of course, increase substantially from $N_b=16$ to $N_b=22$, the bright state is no longer nearly degenerate with as many states. The states in the interior of the $N_b=22$ polyad, with $v_4 \approx v_5$, are coupled very strongly with each other, both due to large matrix elements and small zero-order energy differences, but the bright state is coupled less strongly into this bath of states by virtue of its zero-order energy.

This diagram also provides insight into the strong, quasiperiodic exchange of energy between the *cis* and *trans* bending modes that was observed in the plot of $\langle v_b(t) \rangle$ for this polyad (Fig. 3). The bright state $(0,0,0,22^0,0^0)$, can be observed to be nearly degenerate with $(0,0,0,4^0,18^0)$, $(0,0,0,4^{+2},18^{-2})$, and $(0,0,0,4^{+4},18^{-4})$. Although the bright state is not coupled directly to these states *via* the known anharmonic resonances, vibrational excitation can be expected to flow indirectly but strongly from the *trans* bend end of the polyad to the *cis* bend end *via* a chain of Darling-Dennison resonances through the states with $v_4 \approx v_5$. Figure 7 underscores this point by plotting the survival probability of the bright state (dotted line) along with the time-dependent squared projection of the wave packet onto the $(0,0,0,0^0,22^0)$ zero-order state (solid line). During the first 1 ps of the dynamics, nearly 20% of the vibrational excitation is transferred to the pure *cis* bending zero-order state, at the troughs of the survival probability of the pure *trans* bending bright state.

This strong transfer of vibrational excitation from one end of the polyad to the other is remarkable because the $(0,0,0,22^0,0^0)$ and $(0,0,0,0^0,22^0)$ zero-order states are coupled only very indirectly to each other, by a minimum of 11 quartic anharmonic resonances ($\Delta v=44!$) through other zero-order states. At a qualitative level, the magnitude of the anharmonic resonances at $\sim 15\,000$ cm^{-1} is responsible for the strength of the transfer of energy, and the approximate symmetry of the zero-order states, such that

$$E_{(0,0,0,v_4{}^{l_4},v_5{}^{-l_4})} \approx E_{(0,0,0,v_5{}^{l_4},v_4{}^{-l_4})},$$

is largely responsible for the regular, quasiperiodic nature of this exchange during the first 1-2 ps. We will explore this strong exchange of energy between the *trans* and *cis* normal modes at a deeper level in a forthcoming publication,[29] in which we demonstrate that a local mode model of the pure bending dynamics of acetylene is appropriate at high internal energy. The $N_b=22$ polyad is particularly well-described by a local mode model (as is $N_b=24$, which we have not considered in this paper, because it has not yet been identified experimentally), and it can be demonstrated that exchange of energy between *trans* and *cis* can approach 100% as the molecule approaches the pure local bending limit.

VII. CONCLUSION

The existence of the $N_s=v_1+v_2+v_3$ polyad quantum number in the acetylene $\tilde{X}$ state implies the existence of a class of eigenstates (those with $N_s=0$) that to a good approximation involve no excitation in the stretching modes of the molecule. We have reported previously[2] the application of numerical pattern recognition to our acetylene $\tilde{A}\,{}^1A_u \rightarrow \tilde{X}\,{}^1\Sigma_g^+$ DF data set which has permitted the confident assignment of polyad quantum numbers to observed transitions to up to 15 000 cm^{-1}. In this paper, we have studied in some detail the set of fractionation patterns that this pattern recognition process identified as belonging to the pure bending polyads.

A great deal of information about the pure bending dynamics of acetylene is encoded in the pattern of frequencies and intensities of the transitions to the pure bending eigenstates that are observed experimentally. Our approach to gaining insight into this dynamics in this paper has been to model the observed transitions with an effective Hamiltonian, described in Sec. III, which incorporates all of the anharmonic resonances that are known to couple the bending states of acetylene. This effective Hamiltonian is based closely on previously reported work,[10] but the agreement between model and experiment has been extended to much higher internal energy, such that *all* known pure bending levels of acetylene are fit to $\pm 1.4\ \text{cm}^{-1}$ (1σ), including states with up to 22 quanta of bending excitation and internal energies up to $15\,000\ \text{cm}^{-1}$.

The ability to model the pure bending vibrational levels to such high internal energy affords an opportunity to gain detailed insight into the short-time dynamics of a tetra-atomic molecule with extreme levels of bending excitation. The effective Hamiltonian was investigated using both time-domain (Figs. 3 and 7) and frequency domain (Table III and Fig. 4) formalisms, which together provided a rich, and somewhat surprising, composite picture of the large-amplitude bending dynamics. One major surprise was that the IVR of the bright state with 22 quanta of *trans* bend excitation, at $15\,000\ \text{cm}^{-1}$ of internal energy, demonstrated a regularity that was absent for the bright state with 16 quanta of *trans* bend excitation, at $10\,000\ \text{cm}^{-1}$ of internal energy; in other words, from 10 000 to $15\,000\ \text{cm}^{-1}$ the IVR seemed in some sense to become *simpler*. This observation was explained in terms of the structures of the polyads (Fig. 6).

In a future publication,[29] we will examine the eigen*functions* of the H^{eff} that we developed here. In this forthcoming paper, we will demonstrate that many of the eigenfunctions of the H^{eff} at high internal energy $(>10\,000\ \text{cm}^{-1})$ appear to be quite regular, in the sense that they have clearly identifiable nodal coordinates. However, these nodal coordinates do not correspond to the normal mode coordinates, as they do at lower internal energy. Rather, the eigenfunctions at high internal energy are classifiable as ''local bending'' or ''counter-rotating'' states. These qualitative observations imply that a different basis set may provide a more compact representation of the pure bending dynamics at high internal energy, and we demonstrate that the H^{eff} reported here can be transformed to local bend oscillator coordinates (as opposed to normal mode coordinates) in a manner analogous to Lehmann's treatment of coupled one-dimensional oscillators.[30] The H^{eff} reported here is also currently being studied using the Hamiltonian scaling method of Taylor *et al.*,[31] which permits one to obtain from quantum calculations detailed information about the underlying classical motions.

The development of an analytical potential surface for the bending dynamics of acetylene that can also reproduce the available data up to $15\,000\ \text{cm}^{-1}$ would be highly desirable. Normally, the refinement of a potential surface for a polyatomic molecule against experimental data to such high internal energy would be a very difficult task, but the relatively low dimensionality of the acetylene bending system, combined with the existence of an extensive, rigorously calibrated data set, may make such a task feasible. Recently, McCoy and Sibert have reported the development of a new adiabatic bending potential surface for acetylene, which has shown promise for matching experimental results below $\sim 10\,000\ \text{cm}^{-1}$,[32,33] and we hope that this work will spur further efforts to develop potential surfaces for acetylene with spectroscopic accuracy at high internal energy.

ACKNOWLEDGMENTS

This research has been supported by DOE Grant No. DE-FG0287ER13671. One of the authors (M.P.J.) thanks the Department of the Army for support under a National Defense Science and Engineering Graduate Fellowship.

[1] S. A. B. Solina, J. P. O'Brien, R. W. Field, and W. F. Polik, J. Phys. Chem. **100**, 7797 (1996).

[2] J. P. O'Brien, M. P. Jacobson, J. J. Sokol, S. L. Coy, and R. W. Field, J. Chem. Phys. **108**, 7100 (1988).

[3] J. Plíva, J. Mol. Spectrosc. **44**, 165 (1982).

[4] M. E. Kellman, J. Chem. Phys. **93**, 6630 (1990).

[5] M. E. Kellman and G. Chen, J. Chem. Phys. **95**, 8671 (1991).

[6] C. Jaffe and M. E. Kellman, J. Chem. Phys. **92**, 7196 (1990).

[7] L. E. Fried and G. S. Ezra, J. Chem. Phys. **86**, 6270 (1987).

[8] M. P. Jacobson, S. L. Coy, and R. W. Field, J. Chem. Phys. **107**, 8349 (1997).

[9] L. Coy, M. P. Jacobson, and R. W. Field, J. Chem. Phys. **107**, 8357 (1997).

[10] M. Abbouti Temsamani, M. Herman, S. A. B. Solina, J. P. O'Brien, and R. W. Field, J. Chem. Phys. **105**, 11 357 (1996).

[11] M. Abbouti Temsamani and M. Herman, J. Chem. Phys. **102**, 6371 (1995).

[12] Note that the peak at $8945\ \text{cm}^{-1}$ does not belong to the $N_s = 4$, $N_{\text{res}} = 14$ polyad, as speculated previously.

[13] W. H. Press, S. A. Teukolsky, W. T. Vetterling, and B. P. Flannery, *Numerical Recipes in FORTRAN*, 2nd ed. (Cambridge University Press, Cambridge, 1992).

[14] R. J. Bell and P. Dean, Discuss. Faraday Soc. **50**, 55 (1970).

[15] G. M. Stewart and J. D. McDonald, J. Chem. Phys. **78**, 3907 (1983).

[16] D. S. Perry, J. Chem. Phys. **98**, 6665 (1993).

[17] D. M. Leitner and P. G. Wolynes, Chem. Phys. Lett. **258**, 18 (1996).

[18] D. M. Leitner and P. G. Wolynes, J. Phys. Chem. **101**, 541 (1997).

[19] D. M. Leitner and P. G. Wolynes, J. Chem. Phys. **105**, 11 226 (1996).

[20] K. S. J. Nordholm and S. A. Rice, J. Chem. Phys. **61**, 203 (1974).

[21] E. J. Heller, Phys. Rev. A **35**, 1360 (1987).

[22] E. J. Heller, J. Chem. Phys. **72**, 1337 (1980).

[23] L. Kaplan and E. J. Heller, Physica D (in press).

[24] G. Hose, A. Yogev, and R. M. J. Benmair, Chem. Phys. **102**, 365 (1986).

[25] Y. S. Choi and C. B. Moore, J. Chem. Phys. **94**, 5414 (1991).

[26] G. Hose and H. S. Taylor, Chem. Phys. **84**, 375 (1984).

[27] P. Brumer and M. Shapiro, Adv. Chem. Phys. **70**, 365 (1998).

[28] J. E. Gambogi, J. H. Timmermans, K. K. Lehmann, and G. Scoles, J. Chem. Phys. **99**, 9314 (1993).

[29] M. P. Jacobson, J. P. O'Brien, R. J. Silbey, and R. W. Field (in preparation).

[30] K. K. Lehmann, J. Chem. Phys. **79**, 1098 (1983).

[31] J. Main, C. Jung, and H. S. Taylor, J. Chem. Phys. **107**, 6577 (1997).

[32] E. L. Sibert, III, and A. B. McCoy, J. Chem. Phys. **105**, 459 (1996).

[33] A. B. McCoy and E. L. Sibert, III, J. Chem. Phys. **105**, 469 (1996).